



Aging behavior of lithium iron phosphate based 18650-type cells studied by *in situ* neutron diffraction

Neelima Paul ^{a,*}, Johannes Wandt ^{b,1}, Stefan Seidlmayer ^a, Sebastian Schebesta ^c, Martin J. Mühlbauer ^{a,d,e}, Oleksandr Dolotko ^a, Hubert A. Gasteiger ^b, Ralph Gilles ^a

^a Heinz Maier-Leibnitz Zentrum (MLZ), Technische Universität München, 85747 Garching, Germany

^b Chair of Technical Electrochemistry, Technische Universität München, 85748 Garching, Germany

^c VW-VM Forschungsgesellschaft mbH & Co. KG, 73479 Ellwangen, Germany

^d Institute for Applied Materials (IAM), Karlsruhe Institute of Technology (KIT), Hermann-von-Helmholtz-Platz 1, 76344 Eggenstein-Leopoldshafen, Germany

^e Helmholtz-Institute Ulm for Electrochemical Energy Storage (HIU), P.O. Box, 76021 Karlsruhe, Germany

H I G H L I G H T S

- Aging in MCMB/LFP and NC/LFP cells was investigated by neutron diffraction.
- NC/LFP cell lost capacity on storage whereas the MCMB/LFP cell showed no loss.
- After 4750 cycles, the relative capacity losses were much lower for the MCMB/LFP cell.
- Entire capacity loss upon formation, cycling and storage is due to active lithium loss.
- Structural degradation and active material isolation could be excluded.

A R T I C L E I N F O

Article history:

Received 12 November 2016

Received in revised form

13 January 2017

Accepted 31 January 2017

Available online 8 February 2017

Keywords:

Lithium-ion batteries

Neutron diffraction

In-situ studies

Aging

Graphite

Lithium iron phosphate

A B S T R A C T

The aging behavior of commercially produced 18650-type Li-ion cells consisting of a lithium iron phosphate (LFP) based cathode and a graphite anode based on either mesocarbon microbeads (MCMB) or needle coke (NC) is studied by *in situ* neutron diffraction and standard electrochemical techniques. While the MCMB cells showed an excellent cycle life with only 8% relative capacity loss (i.e., referenced to the capacity after formation) after 4750 cycles and showed no capacity loss on storage for two years, the needle coke cells suffered a 23% relative capacity loss after cycling and a 11% loss after storage. Based on a combination of neutron diffraction and electrochemical characterization, it is shown that the entire capacity loss for both cell types is dominated by the loss of active lithium; no other aging mechanisms like structural degradation of anode or cathode active materials or deactivation of active material could be found, highlighting the high structural stability of the active material and the excellent quality of the investigated cells.

© 2017 Elsevier B.V. All rights reserved.

1. Introduction

Since their commercialization by Sony in 1991, Li-ion batteries have become the main power source for portable consumer electronics. Due to their constant improvement in terms of cost, energy density and lifetime [1,2], Li-ion batteries have also started spreading into new markets like hybrid electric (HEV) and electric

vehicles (EV) or grid storage within the last couple of years [3,4]. To be cost competitive with other energy storage technologies, the lifetime of Li-ion cells is a critical value: while a life time of 2–3 years is sufficient for most consumer electronic applications [5], a lifetime of 15 years and cycle life over 1000 charge/discharge cycles are required for battery electric vehicles (BEVs) [6]; even longer cycle life of over 5.000–10.000 charge/discharge cycles is required for grid storage applications [7]. In order to reach these targets, a detailed understanding of the undesired side reactions contributing to capacity fading is mandatory. Recently, a broad variety of analytical techniques has been used to unravel the underlying

* Corresponding author.

E-mail address: Neelima.Paul@frm2.tum.de (N. Paul).

¹ Authors N.P and J.W contributed equally to this work.

chemical, physical and mechanical processes taking place during charge, discharge (cyclic aging) and storage (calendar aging) of Li-ion batteries [8]. For many of these analytical techniques, *in situ/in operando* setups have been developed which offer several advantages in comparison to *ex-situ* analysis: i) enabling the detection of unstable reaction intermediates [9] or phases [10], ii) avoiding the risk of altering the sample, e.g., the state of charge or the oxidation state, during sample preparation [11], and iii) offering the possibility to continue with cell cycling following the analysis. Most spectroscopy and microscopy based *in situ/in operando* techniques require special cell designs which are transparent for either electromagnetic waves, magnetic fields, and/or electrons [12–15], thus rendering them unsuitable for the investigation of commercial Li-ion cells with generally impenetrable metal casing/housing. There are, however, degradation mechanisms which can only be studied in large-format cells, e.g., effects related to current collector tab positioning [16], cell geometry [17], or inhomogeneous heat distribution [18,19]. A powerful analytical technique for the *in situ/in operando* study of commercial Li-ion cells is neutron diffraction. Rietveld analysis of neutron diffractograms can be used to determine the atomic structure, lattice parameters, and particle size of crystalline anode (e.g. graphite) and cathode active materials (e.g. spinels, layered metal oxides, or phospho-olivines). In this respect, an important advantage of neutron diffraction over X-ray diffraction (XRD) is the higher penetration depth of neutrons in comparison to X-rays, making neutron diffraction truly bulk sensitive and suitable for large cell formats, whereas XRD is only suitable for thin samples [20]. Furthermore, neutron diffraction shows a much higher sensitivity for light elements like lithium than XRD.

Only few *in situ/in operando* neutron diffraction studies on commercial Li-ion cells have been published so far, typically based on cells with graphite anodes and a variety of cathode active materials like LiCoO₂ (LCO) [16,21–24], LiMn₂O₄ (LMO) [25], LiMn_{0.33}Co_{0.33}Ni_{0.33}O₂ (NMC) [10,16,26,27], and LiFePO₄ (LFP) [16,28–30]. These have focused on topics like structural changes within the cathode active material [22,26], metal doping [29,30], local inhomogeneities [16,25,31], or lithium plating on graphite [27]. While there are neutron diffraction studies on cell aging for commercial graphite/LCO cells [23,24], to the best of our knowledge no such data is available for graphite/LFP cells.

In this work, we carry out a detailed investigation of the aging mechanism in commercially produced 18650-type cells with a graphite/LFP cell chemistry. A total of four cells are investigated in this study which differ either in the type of graphite used as anode active material – mesocarbon microbeads (MCMB) versus needle coke (NC) – or in the cell history. One cell of each graphite anode material was cycled for 4750 cycles at a C-rate of 1 h^{−1} at 23 °C and one cell was stored for about two years at 20% state-of-charge (SOC) at 23 °C. For all four cells we systematically compare the electrochemically determined remaining discharge capacity with the active lithium inventory derived from *in situ* neutron diffraction. With this approach it is possible to differentiate several aging mechanisms, namely i) active lithium loss, ii) particle isolation, further on referred to as particle deactivation, due to loss of ionic and/or electronic contact, and, iii) destruction of bulk electrode material (metal dissolution or irreversible phase transformation). Loss of active lithium has frequently been described to occur in Li-ion cells and may have several reasons, for example ongoing SEI formation or irreversible Li-plating [32,33]. Active lithium loss can be identified if the loss of active lithium inventory measured by neutron diffraction corresponds to the electrochemically determined discharge capacity loss. The second main capacity fading mechanism is particle deactivation, resulting in an effective loss of active material. This can either be caused by the loss of ionic contact due to gassing [34], drying out [35], or pore blocking [36] or by the

loss of electronic contact due to particle delamination from the current collector [10,18] or particle cracking [37]. Particle deactivation has been observed in previous studies in aged commercial Li-ion cells by the presence of lithiated “uncharged” cathode active material [25] and/or of totally unlithiated graphite anode active material in charged cells [23,25]. The third main capacity fading mechanism is the chemical destruction of electrode active material, which could either be due to an irreversible phase transformation or to transition metal dissolution. Examples of the former are the conversion of layered LCO to spinel LCO [22] or the destruction of the spinel structure of LiMn₂O₄ [25] upon cycling. Phase transformations can easily be recognized by the appearance of new peaks in the neutron diffractograms which cannot be assigned to the original electrode materials. Transition metal dissolution has frequently been linked to capacity fading of Li-ion cells. It has been reported that under certain circumstances 3–4% of the iron can dissolve from LFP active material which would cause a direct and stoichiometric capacity loss [38]. If cathode active material loss due to transition metal dissolution is occurring to a significant extent, the observed lithium inventory would stay constant while the electrochemically determined remaining capacity would decrease. The dissolution of transition metals from the cathode can also indirectly contribute to the capacity fading of Li-ion cells by catalyzing electrolyte reduction at the graphite anode, causing a loss of active lithium and an increase in cell impedance [39]. As this is a catalytic process, already a very small amount of transition metal dissolution, whose corresponding direct stoichiometric capacity loss would be negligible, can cause a substantial capacity loss [40]. Note that in the framework of this study, the transition metal triggered capacity loss on the anode side would be observed as increased active lithium loss, rather than constituting an independent capacity loss mechanism.

2. Experimental

2.1. Cell information

The cylindrical 18650-type graphite/LFP prototype cells were provided by the battery producer (VW-VM Forschungsgesellschaft mbH & Co. KG, a joint venture between Volkswagen and VARTA Microbattery GmbH). Each cell consisted of a LFP cathode, an organic carbonate based electrolyte with LiPF₆ as conducting salt, a standard polyolefin separator, and a graphite anode made of either mesocarbon microbeads or needle coke. In both types of cells identical LFP cathodes were used. The cathode consisted of 90 wt% active material, 5 wt% binder and 5 wt% conductive additive (3 wt% graphite and 2 wt% SuperC) and was coated on both sides of an Al-foil current collector; all cells contained a total of 10.75 g LFP (2.4 wt % carbon coating), resulting in a theoretical cell capacity Q_{theo} of 1.678 Ah (based on an achievable capacity of 160 mAh g_{LFP}^{−1}, see Supporting Information). The amount of anode active material was adjusted to obtain an anode/cathode capacity ratio of 1.25 considering the specific capacities of MCMB (330 mA g^{−1}) and needle coke (349 mAh g^{−1}). The anodes consisted of 97 wt% of graphite active material, 2.5 wt% binder and 0.5 wt% conductive additive coated on both sides of a Cu-foil current collector. The BET surface area of the pure powders was 2.4 m² g^{−1} for MCMB and 1.9 m² g^{−1} for needle coke.

After the cell assembly, all cells were subjected to a proprietary formation procedure and the thus obtained preformed cells were then either stored for two years (at 20% SOC and 23 °C) or cycled for 4750 cycles (at a C rate of 1 h^{−1} at 23 °C) by the battery producer. Of each cell type, three identical cells were cycled. The observed discharge capacities for the three identical cells were always within 0.4% for both cell types, exemplifying the very good reproducibility

of the commercially produced cells. After long term cycling/storage, four cells (cycled vs. stored and MCMB vs. needle coke) were examined by neutron diffraction and subjected to further electrochemical characterization like impedance spectroscopy and cycling at different C-rates. The total time span between cell assembly and the here described neutron diffraction and electrochemical experiments was about 24 months. No neutron diffraction analysis was conducted directly after cell formation, as this study was initiated only after the cycling/storage experiments had been completed. Fig. 1 gives an overview of the chronological sequence of electrochemical and neutron diffraction experiments as well as the nomenclature used within this work to refer to the different points in time at which the various tests were conducted. The term “pristine cell” refers to the cells directly after assembly before formation (with the theoretical capacity of 1.678 Ah), whereas after formation the cells are called “preformed cell”. This distinction is crucial because the major capacity fading already occurs during the formation cycles, as discussed later. After the long term cycling/storage tests, the cells are referred to as “cycled cells” and “stored cells”, respectively.

2.2. Neutron diffraction

The neutron powder diffractograms were measured in Debye-Scherrer geometry under ambient conditions at the high-resolution powder diffractometer SPODI, MLZ Garching [41]. Neutrons with wavelength of $\lambda = 1.5483 \text{ \AA}$ from the Ge (551) monochromator were incident on the cell with a rectangular illumination cross section of $40 \times 30 \text{ mm}^2$. The scattered neutrons were collected by a neutron detector array of 80 vertical position sensitive detectors [41,42]. The cells were rotated around their cylindrical axis during the measurement to reduce texture effects in the diffraction pattern. Five diffractograms were measured for each cell with an acquisition time of about 1 h 10 min each, depending on monitor rate/neutron flux. Therefore, the total integration time for the averaged plotted diffractograms for each cell was approximately 6 h. The edges of the cell (about 10 mm) at the top and bottom were not illuminated by the neutron beam. Thus, averaged information from the central part of the cylindrical cell (central 45 mm of total 65 mm height) is obtained from these diffractograms. Pictures of the powder diffractometer, the mounted cells as well as a schematic of the neutron diffraction set-up can be seen in Fig. 2. Multiphase, sequential Rietveld refinement of structural models for the neutron diffraction data has been carried out with the FullProf software package [43]. The instrumental resolution function was determined with a $\text{Na}_2\text{Ca}_3\text{Al}_2\text{F}_{14}$ reference material and used to calculate half widths of the reflections. A Thompson-Cox-Hastings pseudo-Voigt function was used to describe the peak profile shape. A linear interpolation between selected data points in non-overlapping regions was used to fit the background. For the steel housing and the current collectors, a structure independent (Le Bail) profile fit was used due to the strong preferred orientations of crystallites in these materials. This was done in

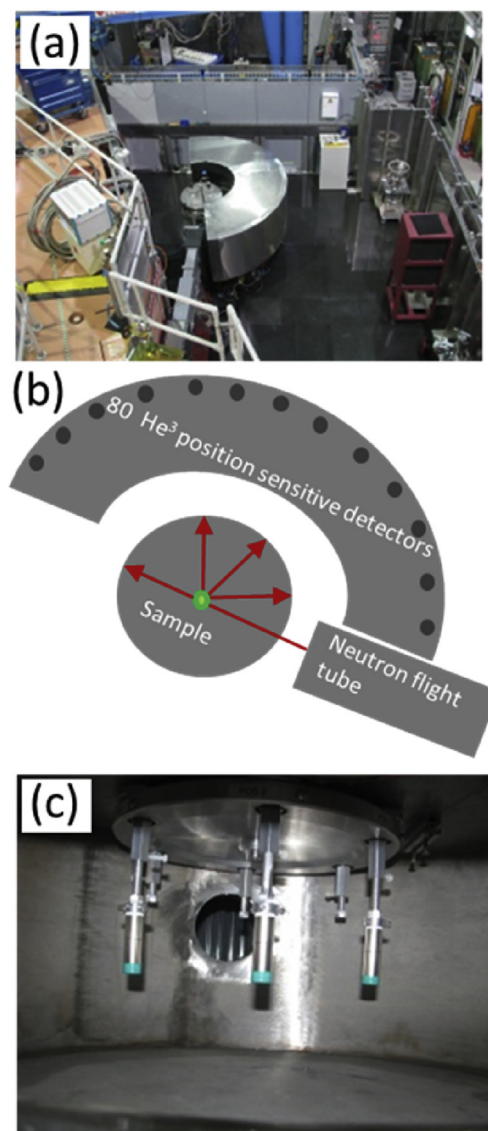


Fig. 2. a) The neutron diffractometer SPODI with the Ge (551) monochromator and the detector array around the sample chamber, b) schematic representation of the experimental set-up, and, c) the positioning of the cylindrical 18650-type Li-ion cells inside the sample changer.

order to obtain a better quality multi-phase pattern refinement of the neutron diffractogram.

2.3. Electrochemical techniques

The formation procedure of the cells was carried out by the battery producer; details regarding the formation procedure are

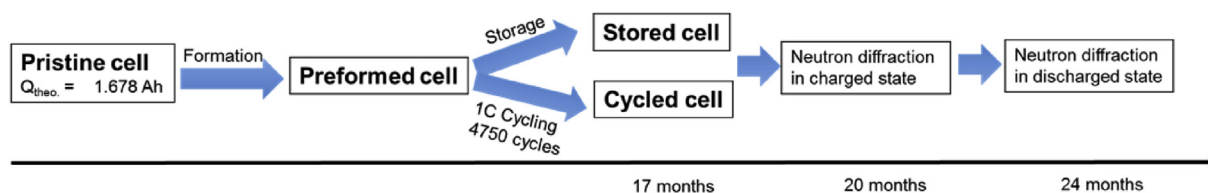


Fig. 1. Schematic showing the chronological sequence of electrochemical and neutron diffraction experiments as well as the nomenclature used to refer to the different conditions of the cells.

proprietary and are thus not being disclosed. After formation, the MCMB cells had a reversible capacity of 1.230 Ah and the needle coke cells of 1.150 Ah; all C-rates used within this work relate to these capacities of the preformed cells. Long term cycling (ca. 4750 cycles) at 23 °C was performed by the battery producer with a CCCV charge to 3.6 V (constant current (CC) charging at 1C to 3.6 V, followed by a constant voltage (CV) hold at 3.6 V until a current corresponding to C/20 is reached) and a CC discharge to 2.0 V with a rate of 1C using a Maccor battery tester. Prior to the neutron diffraction experiments in the charged state, the cells were charged with the above described cycling procedure; on the other hand, prior to neutron diffraction experiments in the discharged state, the cells were discharged with a C/5 rate followed by a CV hold at 2.0 V (with a C/20 cut-off) in order to ensure that the cells are fully discharged. Potentiostatic electrochemical impedance spectroscopy (PEIS) was carried out with a 5 mV perturbation amplitude in the frequency range from 300 kHz to 100 mHz on fully charged cells. Impedance spectra were fitted with the EC-Lab software package (Biologic, France) to determine high frequency and charge transfer resistances. Charging and discharging before the neutron diffraction experiments and the impedance spectroscopy was carried out with a Biologic VMP3 potentiostat.

2.4. Morphology of MCMB and needle coke

The scanning electron microscopy (SEM) images of the pristine MCMB and NC powder were recorded on a JEOL JCM-6000 (secondary electron imaging, 15 kV accelerating voltage). The MCMB powder, shown in Fig. 3a and b, consists of spherical particles with

an average particle diameter of approximately 10 μm and the surface of these particles shows significant roughness in the sub-micrometer range. In contrast, the needle coke powder shown in Fig. 3c and d, consists of anisotropic flake shaped particles with a larger particle size, broader size distribution and a rather smooth particle surface in comparison to the MCMB.

3. Results

3.1. Electrochemical characterization

Table 1 shows the absolute discharge capacities measured at a 1C rate and normalized capacities with respect to the pristine ($Q_{\text{dis}}/Q_{\text{theo}}$) and preformed capacities ($Q_{\text{dis}}/Q_{\text{preformed}}$) for the MCMB and NC cells in their preformed, stored and cycled states, whereby $Q_{\text{theo}} = 1.678 \text{ Ah}$ is based on the theoretical LFP capacity of $160 \text{ mAh g}^{-1}_{\text{LFP}}$ as previously described.

Fig. 4a shows the relative change of the discharge capacities of the graphite/LFP cells as a function of time and cycle number (CC charge at 1C with a CV hold at 3.6 V until a C/20 cut-off and 1C discharge to 2.0 V at 23 °C), normalized by the discharge capacity of the preformed cells (1.230 Ah for MCMB and 1.150 Ah for the NC; see Table 1). The cycled MCMB cell (light green line) shows a linear drop in capacity versus cycle number, with a relative capacity loss of 8.2% over 4750 cycles; in contrast, the capacity fading rate for the needle coke cell (light blue line) is substantially higher during the initial 1000 cycles before gradually leveling off to a capacity fading rate which is similar to the MCMB cells, resulting in an overall relative capacity loss of 23.1% over 4750 cycles. After two years of

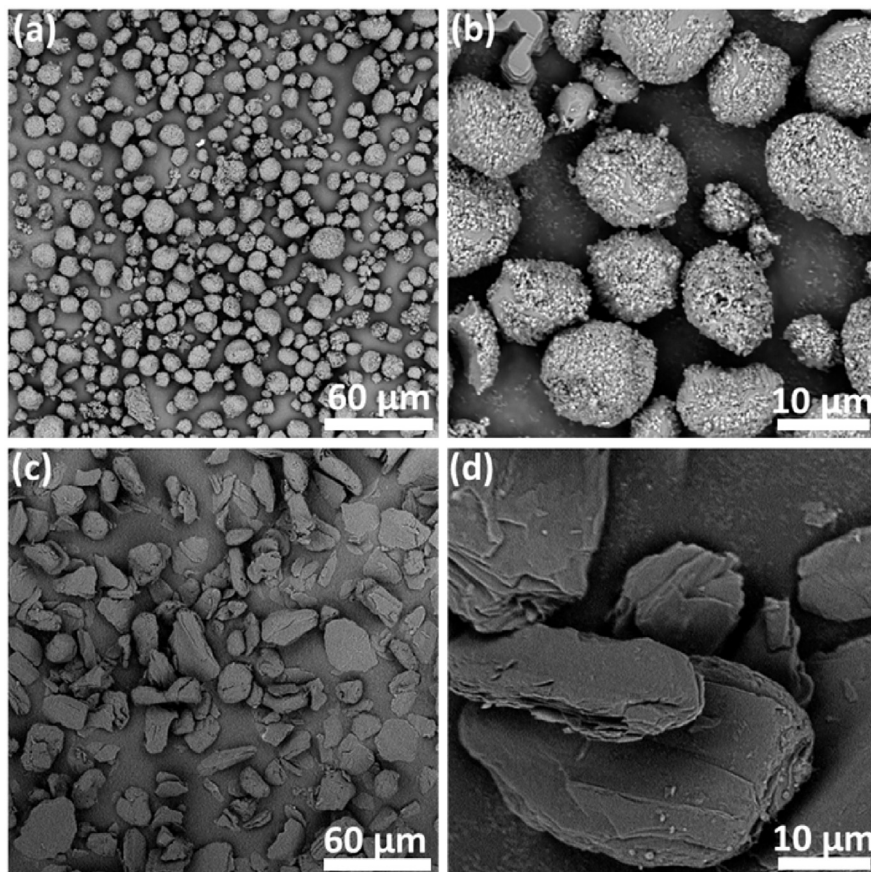


Fig. 3. a) and b) show SEM images of the pristine MCMB powder, whereas c) and d) show SEM images of the pristine needle coke powder at two different magnifications.

Table 1

Absolute discharge capacities (Ah) measured at a 1C rate (Q_{dis} ; 2nd column), as well as the capacities normalized either to the theoretical capacity ($Q_{\text{theo}} = 1.678$ Ah) of the LFP capacity-limited cells ($Q_{\text{dis}}/Q_{\text{theo}}$; 3rd column) or to the capacity after formation ($Q_{\text{dis}}/Q_{\text{preformed}}$; 4th column). The 5th column shows capacity loss after storage or cycling in comparison to the capacity of the preformed cell.

State of cells	Q_{dis} [Ah]	$Q_{\text{dis}}/Q_{\text{theo}}$ [%]	$Q_{\text{dis}}/Q_{\text{preformed}}$ [%]	Relative Q-change [%]
Preformed MCMB	1.230	73.3	≈ 100.0	
Stored MCMB	1.249	74.4	101.5	+1.5
Cycled MCMB	1.130	67.3	91.8	−8.2
Preformed NC	1.150	68.5	≈ 100.0	
Stored NC	1.025	61.1	89.1	−10.8
Cycled NC	0.884	52.8	76.9	−23.1

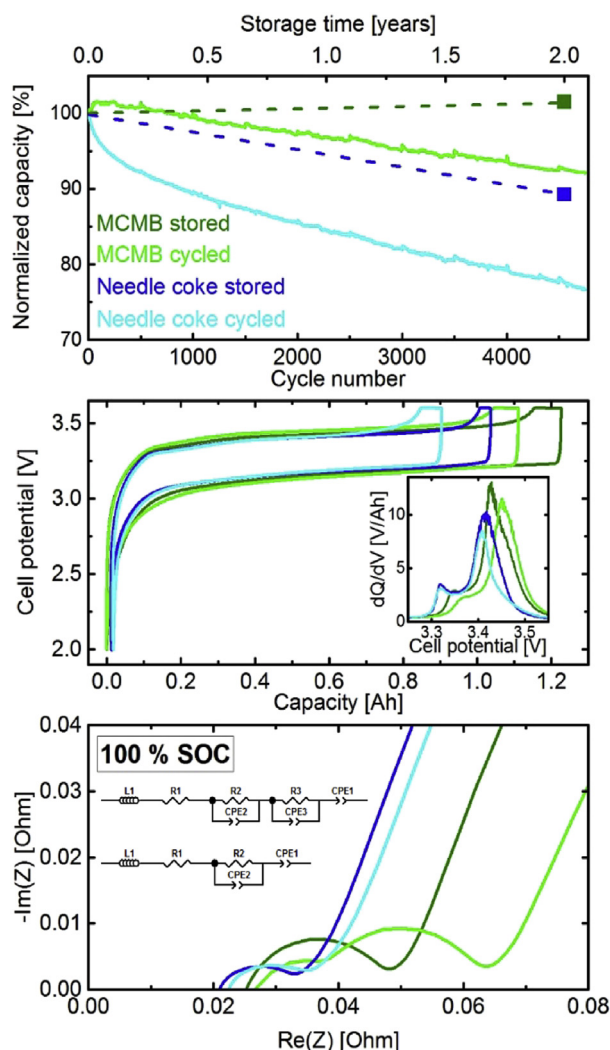


Fig. 4. **a)** solid lines: Relative discharge capacities (referenced to the capacity after formation; see Table 1) of the 18650 graphite/LFP cells at 23 °C as a function of cycle number (CC charge at 1C to 3.6 V with a CV hold at 3.6 V until a C/20 current cut-off and 1C CC discharge to 2.0 V); solid symbols: relative capacity loss after storage at 20% SOC and 23 °C for 2 years (the dashed lines are a guide to the eye). **b)** Potential profiles recorded with a 1C CCCV charge/1C CC discharge rate at 23 °C after the long term storage or cycling experiments; the inset shows the corresponding dQ/dV plot for the charging curves; **c)** PEIS of the long term stored and cycled cells acquired at 100% SOC (5 mV perturbation at frequencies between 300 kHz and 0.1 Hz) and corresponding equivalent circuits.

storage at 20% SOC and 23 °C for 2 years, the relative capacity of the MCMB cell increased by 1.5% (dark green square), whereas it decreased by 10.8% for the needle coke cell (dark blue square). The

potential profiles of the stored and cycled cells (Fig. 4b) are typical for LFP/graphite cells and show features which can be assigned to the staging behavior of the graphite anode. The polarization is slightly higher for the two MCMB cells than for the two needle coke cells. This is more apparent in the dQ/dV plot of these data (inset Fig. 4b), which shows that there is a cycling induced polarization increase (comparing the cycled vs. the stored cell) of approximately 23 mV for the MCMB anode material, whereas there is no noticeable difference in the polarization for the needle coke cells.

Potentiostatic electrochemical impedance spectroscopy (PEIS) data together with the equivalent circuits used for fitting the PEIS data are depicted in Fig. 4c. The stored MCMB cell and both needle coke cells were fitted with one R/Q element (as shown in the lower equivalent circuit), while the cycled MCMB cell clearly displayed two semi-circles in the Nyquist plot and was thus fitted with two R/Q elements (as shown in the upper equivalent circuit). All four cells show similar high frequency resistances of about 20 mΩ and a first semi-circle which can be assigned to predominantly reflect the charge-transfer resistance of the graphite anode (as shown recently [44], the semi-circle in the full-cell impedance of an LFP/graphite cell mostly derives from the graphite anode). This apparent charge-transfer resistance is ≈ 26 mΩ and ≈ 29 mΩ for the stored and cycled MCMB cells versus only ≈ 14 mΩ and ≈ 15 mΩ for the stored and cycled needle coke cells. The higher charge transfer resistance of the MCMB cells in comparison to the needle coke cells is in line with the higher polarization observed in the potential profiles (Fig. 4b). The cycled MCMB cell also shows an additional smaller semicircle with a resistance of ≈ 16 mΩ which is not present in the stored MCMB cell. Based on its diameter (16 mΩ) and the frequency of its maximum (2710 Hz), the capacitance of this additional semi-circle equals 3700 μF. Considering a typical double layer capacitance in the order of 10 μF cm^{−2}, an effective interfacial area of 370 cm² can be calculated, which is in good agreement with the geometric area of the current collector foils in a 18650 cell but significantly smaller than the electrode material surface area (140 · 10³ cm² for a graphite mass of 7 g and a BET area of 2 m² g^{−1}) [45,46]. Accordingly, the additional semi-circle in the cycled MCMB cell can most likely be assigned to an increased contact resistance between the active material and the current collector foil. For the cycled MCMB cell this additional resistance of ≈ 16 mΩ corresponds to an additional IR drop of ≈ 20 mV at a current of 1.230 A (= 1C rate), which is very close to the observed polarization increase of 23 mV for the cycled MCMB cell in comparison to the stored MCMB cell (Fig. 4b).

Furthermore, to test whether the slight polarization increases affect the discharge capacities, all cells were cycled with a C/50 rate between 2.0 and 3.6 V (data not shown). For all four cells, the discharge capacities in the C/50 cycle are identical with the 1C discharge capacities within 5%, implying that resistive effects (often associated with capacity roll-over fading) [36] do not contribute to capacity fading.

3.2. Neutron diffraction

In situ neutron diffraction is used to obtain detailed structural information about the anode and cathode materials without opening the cell. It has to be noted, however, that averaged information from the central part of the cylindrical cell (central 45 mm of total 65 mm height) is obtained. From the neutron diffraction data it is possible to identify crystalline phases in the Li-ion cells and also to calculate their respective weight fractions and lattice parameters. A high background is observed for all cells due to the incoherent scattering of neutrons by the hydrogen atoms present in the organic electrolyte and separator. This background has no angular dependence and is similar for both cells irrespective of their state of charge.

3.2.1. Discharged cell

Neutron diffraction data for the four different cells in their discharged state is presented in Fig. 5, along with their Rietveld refinements. The steel casing as well as the Al and Cu current collectors show their respective reflections with similar intensities in all four cells. Reflections of LiFePO_4 and graphite, as expected for a lithiated cathode and a delithiated anode, are also present in all four cells. However, reflections of FePO_4 are also present in all cells, implying that a significant portion of FePO_4 in the cathode has not been converted to LiFePO_4 , even after fully discharging the cell. From Rietveld refinement of the neutron diffraction data shown in

Fig. 5, weight fractions of LiFePO_4 and FePO_4 were obtained and converted into their molar ratios: LFP/FP molar ratios are 75:25 for the stored MCMB cell, 67:33 for the cycled MCMB cell, 58:42 for the stored needle coke cell, and 55:45 for the cycled needle coke cell. In all cells, the total absence of peaks belonging to lithiated graphite (Li_xC_6 with $x \neq 0$) is an indication for the complete extraction of lithium from the anode during discharging. This clearly proves the absence of regions with inactive lithiated graphite (due to particle isolation or electrode delamination, etc.).

It should be noted that due to the extremely weak and multiple reflections of the LiFePO_4 and FePO_4 phases (see Fig. 5c and f), the purpose of the refinement was not to determine lattice parameters with high accuracy, but rather to calculate and compare the molar fractions of the LiFePO_4 and FePO_4 phases in the discharged state of the stored and cycled cells. Still, the structural stability of the LFP cathode material is confirmed by the constant and fixed angular position of the LiFePO_4 (221) reflections, as exemplified in Fig. 5c and f. Within the accuracy of the experiment, the lattice parameters of cathode (LiFePO_4 and FePO_4) remain unchanged for all cells. We take the maximum error value obtained from the fitting as the general error value for all lattice parameters displayed in Tables 2 and 3.

For the MCMB and needle coke graphites present in the discharged cells it is possible to determine lattice parameters a and c as shown in Table 2. Both lattice parameters are identical for the stored and cycled MCMB cell. The cycled needle coke cell shows a

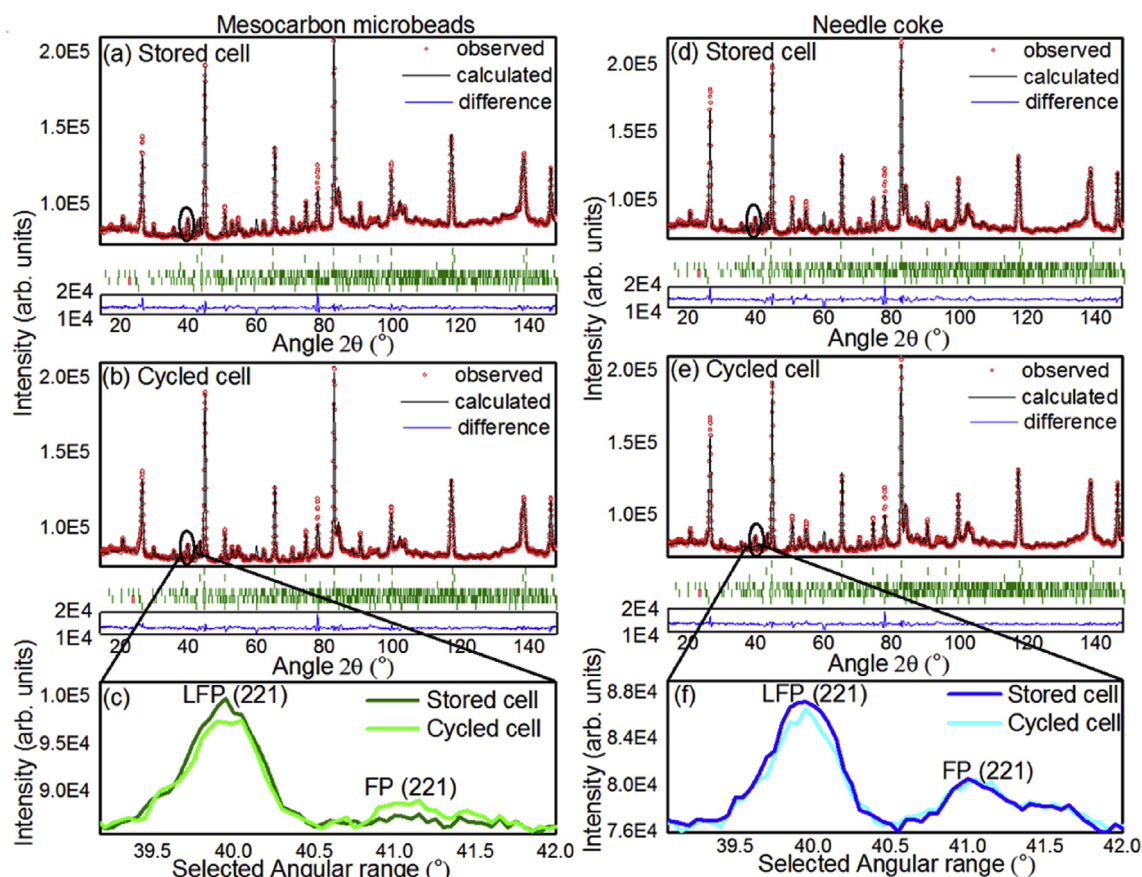


Fig. 5. Neutron diffraction data with full angular range of the graphite/LFP cells measured in the fully discharged state (discharged at a C/5 CC rate to 2.0 V with a CV hold at 2.0 V to a C/20 cut-off). **a)** Stored MCMB cell, **b)** cycled MCMB cell, **d)** stored needle coke cell, **e)** cycled needle coke cell. Experimental data are shown in red circles along with their Rietveld refinements (black line). The blue lines mark the difference between data and fit. Vertical bars (green) above the blue line indicate Bragg reflections corresponding to the crystalline phases in the cell (from top to bottom: Fe, Cu, Al, LiFePO_4 , FePO_4 , and graphite). **c)** and **f)** Selected angular range of neutron diffraction data focusing on the relatively weak LFP (221) reflection and the even weaker FP (221) reflection for the MCMB cells (c) and needle coke cells (f) (these are the only reflections from the cathode active material which do not overlap with reflections from other components). (For interpretation of the references to colour in this figure legend, the reader is referred to the web version of this article.)

Table 2

Lattice parameters for MCMB and needle coke cells as determined by Rietveld refinement of the neutron diffractograms of the discharged cells (data from Fig. 5). Lattice parameters of conventional LCO/graphite cell are also shown for comparison.

State of cells	Graphite- a [Å]	Graphite- c [Å]
Stored MCMB	2.462 ± 0.004	6.756 ± 0.004
Cycled MCMB	2.462 ± 0.004	6.756 ± 0.004
Stored Needle coke	2.462 ± 0.004	6.736 ± 0.004
Cycled Needle coke	2.462 ± 0.004	6.729 ± 0.004
Graphite literature ref. [23]	2.463	6.722

Table 3

Lattice parameters determined by Rietveld refinement of the neutron diffractograms of the charged cells by fitting the data according to the structural model of the LiC_{12} phase. Literature values corresponding to the LiC_{12} phase in LCO/graphite cells are shown for comparison.

State of cells	$\text{LiC}_{12} - a$ [Å]	$\text{LiC}_{12} - c$ [Å]
Stored MCMB	4.294 ± 0.004	7.074 ± 0.004
Cycled MCMB	4.293 ± 0.004	7.070 ± 0.004
Stored Needle coke	4.295 ± 0.004	7.043 ± 0.004
Cycled Needle coke	4.285 ± 0.004	7.037 ± 0.004
Lithiated graphite - literature ref. [23]	4.294 (fresh and fatigued)	7.034 (fresh)/7.038 (fatigued)

slightly reduced lattice parameter c in comparison to the stored cell, the reason of which is not clear. In contrast, an earlier neutron diffraction study found a slight increase of the lattice parameter for a cycled graphite anode [23]. A comparatively larger c parameter for the MCMB based cells in comparison to that in the needle coke and conventional graphite based cells is also observed in the X-ray diffraction pattern of their pristine powders (not shown here).

3.2.2. Charged cell

In the charged state, the cathode is delithiated, whereas the anode is lithiated. The diffraction data of the four cells in the charged state are shown in Fig. 6 along with their Rietveld refinements. In the stored and cycled MCMB cells, reflections of FePO_4 , LiC_6 , and LiC_{12} are clearly visible. From Rietveld refinement, weight fractions of LiC_6 and LiC_{12} were obtained and converted into their molar ratios: $\text{LiC}_6/\text{LiC}_{12}$ molar ratios are 23:77 for the stored MCMB cell and 12:88 for the cycled MCMB cell. In the two needle coke cells, both FePO_4 and LiC_{12} phases are present, whereas the LiC_6 reflections are very weak in the stored and almost absent in the cycled needle coke cell. The different intensities of the LiC_6 phase can be rationalized based on the remaining capacities of the respective cells: LiC_6 corresponds to a $\text{SOC}_{\text{graphite}}$ of 100% and LiC_{12} to a $\text{SOC}_{\text{graphite}}$ of 50%; however, when considering the anode/cathode balancing factor of 1.25, the complete LiC_{12} phase would correspond to an SOC of the cell of $\text{SOC}_{\text{cell}} = 62.5\%$. Accordingly, only at cell capacities above 62.5% referenced to the theoretical cell capacity one would expect to observe the formation of the LiC_6 phase (together with the LiC_{12} phase).

A comparison with Table 1 (3rd column) thus suggests that the LiC_6 phase should be present in the charged state in the stored and cycled MCMB cells ($Q_{\text{dis}}/Q_{\text{theo}}$ of 74.4% and 67.3%, respectively), as indeed is demonstrated by the neutron diffraction data shown in Fig. 6c. On the other hand, the low relative capacities observed in the charged state of the stored and cycled needle coke cells ($Q_{\text{dis}}/Q_{\text{theo}}$ of 61.1% and 52.8%, respectively) should not allow the formation of the LiC_6 phase, which again is confirmed by the neutron diffraction data shown in Fig. 6f. By the same token, at cell capacities below 62.5% one would expect a mixture of LiC_{12} and lithiated graphite of the general composition LiC_x , with $x > 12$ (e.g., LiC_{18} or LiC_{24}). The transition from LiC_6 to LiC_{12} is a two-phase mechanism

resulting in two clearly separated peaks at $2\theta = 24.2^\circ$ and $2\theta = 25.3^\circ$ in the neutron diffractograms, as clearly observed for the MCMB cells in Fig. 6c. The mechanism of the transition from LiC_{12} to lower lithiation degrees (e.g., LiC_{18} , LiC_{24}) is more complicated, and it is still controversially discussed whether it is a combination of several sequential two-phase transitions or rather a continuous single phase mechanism [47,48]. Independent of the underlying mechanism, the further delithiation of LiC_{12} causes a continuous shift of the corresponding reflection to higher angular values, as observed for the cycled needle coke cell (light blue line in Fig. 6f). Due to this more complicated mechanism, it is not possible to extract molar ratios of the different lithiated graphite phases from neutron diffraction for cells in which the LiC_6 phase is not present, as is the case for the cycled and stored needle coke cells.

In all four cells, the absence of any LiFePO_4 peaks within the accuracy of the neutron experiment is an indication for the complete extraction of lithium from the cathode during charging. In addition, all charged cells show a small peak at $2\theta = 26.5^\circ$, which has the same intensity in all four charged cells and an angular position which is overlapping with the C (002) signal of graphite. This peak is not observed/resolved in the discharged state of the cells, because of the high intensity of the C (002) reflection from the delithiated graphite active material. As the relative intensity of this carbon signal is identical for all cells and as its weight fraction matches the amount of conductive carbon present in the cathode (SuperC), one can most likely assign this signal to the conductive carbon in the cathode, which shows negligible lithium intercalation and thus remains unlithiated even in the charged cells. One may note that the shoulder at $2\theta = 25.9^\circ$ is due to the FePO_4 (111) reflection and not due to a LiC_x phase with $x > 12$. Accordingly, the entire MCMB and needle coke present in the anode is lithiated during charge, thus ruling out the presence of electrochemically inactive anode material.

Table 3 shows the lattice parameters of the LiC_{12} phase as determined by Rietveld refinement of the neutron diffraction data shown in Fig. 6 according to the structural model of the LiC_{12} phase. For the MCMB cells there is no difference in lattice parameters between the cycled and the stored cell, confirming the structural stability of the MCMB graphite upon cycling. The reduction in the lattice parameter for the cycled needle coke cell as compared to the stored cell is probably due to the onset of its transition from the LiC_{12} phase to a phase with a lower lithiation degree as discussed above.

3.3. Active lithium content from $Q_{\text{discharge}}$, the $\text{LiFePO}_4/\text{FePO}_4$ ratio, and the $\text{LiC}_6/\text{LiC}_{12}$ ratio

As described in the previous section, the Rietveld refinement of the neutron diffraction data gives the molar ratios of $\text{LiFePO}_4/\text{FePO}_4$ (LFP/FP) for the discharged cells and of $\text{LiC}_6/\text{LiC}_{12}$ for the charged cells (both after cycling and after storage), which are summarized in Table 4. Neutron diffraction experiments could not be carried out for the cells directly after formation (i.e., the preformed cells in Fig. 1), because the formation was done several years prior to the here described neutron diffraction analysis. It is possible to use the molar ratios of LFP/FP and $\text{LiC}_6/\text{LiC}_{12}$ to determine the active lithium inventory (LI). The active lithium inventory equals the amount of electrochemically active lithium, which is either contained in the LFP cathode when the cell is discharged or in the lithiated graphite anode (as phases of LiC_6 , LiC_{12} , etc.) when the cell is charged. The LI can best be expressed as percentage of the initial amount of active lithium, which is introduced into the pristine cell by the LFP cathode.

The thus defined active lithium inventory derived from the LFP/FP ratio of the discharged cells is denoted as $LI_{\text{LFP/FP}}$ and simply

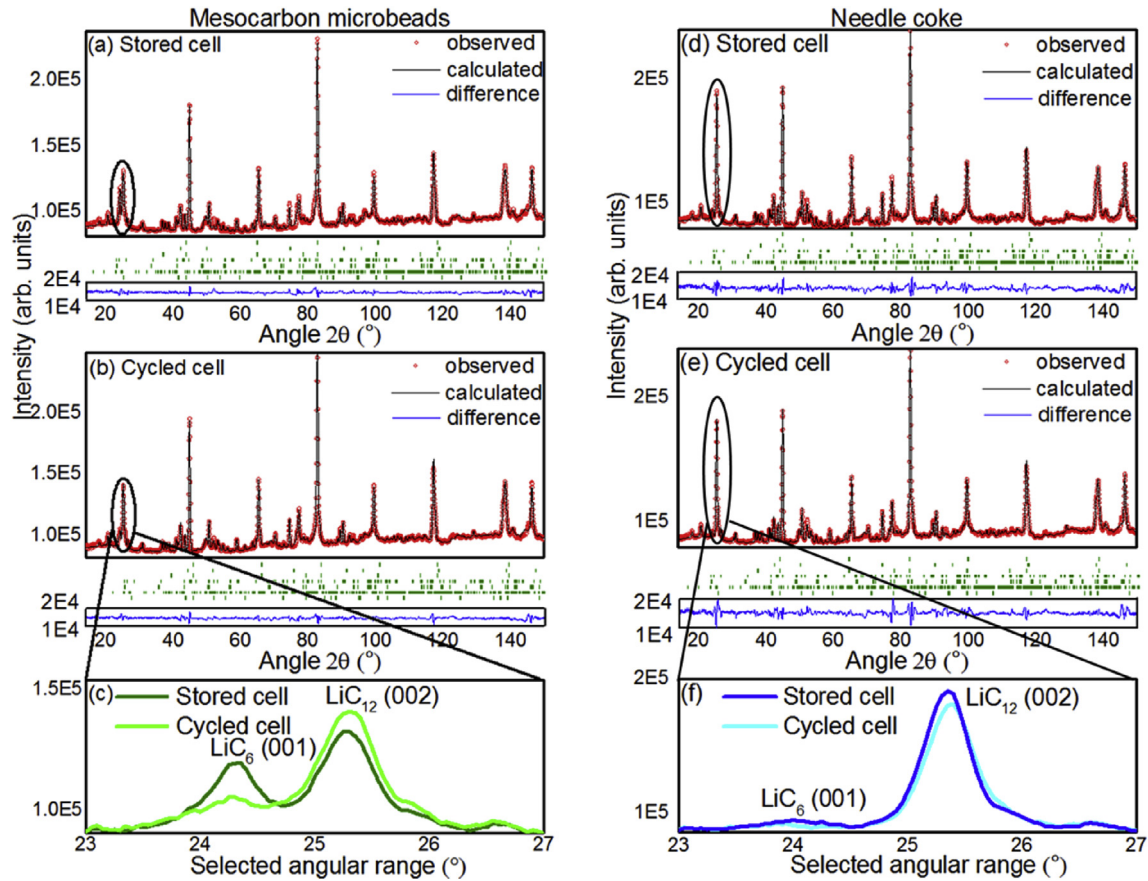


Fig. 6. Neutron diffraction data with full angular range of the graphite/LFP cells measured in the fully charged state (charged at a 1C CC rate to 3.6 V with a CV hold at 3.6 V to a C/20 cut-off). a) Stored MCMB cell, b) cycled MCMB cell, d) stored needle coke cell, e) cycled needle coke cell. Experimental data are shown in red circles along with their Rietveld refinements (black line). The blue lines mark the difference between data and fit. Vertical bars (green) above the blue line indicate Bragg reflections corresponding to crystalline phases in the cell (from top to bottom: Fe, Cu, Al, LiC_{12} , LiC_6 , FePO_4 , and graphite). c) and f) Selected angular range of neutron diffraction data focusing on the LiC_6 (001) and LiC_{12} (002) reflections for the MCMB cells (c) and needle coke cells (f). (For interpretation of the references to colour in this figure legend, the reader is referred to the web version of this article.)

Table 4

Molar ratios of $\text{LiFePO}_4/\text{FePO}_4$ and of $\text{LiC}_6/\text{LiC}_{12}$ for stored and cycled cells, as obtained from refinement of the neutron diffraction data for the discharged cells and the charged cells, respectively. Due to their low remaining capacity, $\text{LiC}_6/\text{LiC}_{12}$ ratios could not be determined for the needle coke cells.

State of cells	$\text{LiFePO}_4/\text{FePO}_4$	$\text{LiC}_6/\text{LiC}_{12}$
Stored MCMB	75/25	23/77
Cycled MCMB	67/33	12/88
Stored Needle coke	58/42	n.a.
Cycled Needle coke	55/45	n.a.

equals

$$L_{\text{LFP/FP}} = y(\text{LFP}) \quad (1)$$

where $y(\text{LFP})$ is the molar fraction of LFP (in %) obtained by *in situ* neutron diffraction analysis of the discharged cells (ranging from 55% to 75%, as shown in Table 4). For example, the molar LFP/FP ratio of 75/25 determined for the stored MCMB cell corresponds to a $y(\text{LFP})$ value of 75% and an active lithium inventory of $L_{\text{LFP/FP}} = 75\%$.

To derive the LI from the anode side is not as straightforward, because over the entire SOC range several different phases of lithiated graphite (LiC_6 , LiC_{12} as well as phases with lower lithium content) [27,48] and a pure graphite phase can be present, so that

the lithium content can only be determined if the fraction of all the different phases present can be quantified. Unfortunately, only the LiC_6 and the LiC_{12} have sufficiently different lattice spacings to allow a deconvolution of their diffraction peaks, while the phases with lower lithium content either have a poorly defined stoichiometry and/or overlap with the LiC_{12} diffraction [27]. Therefore, it is only possible to quantify the content of lithium in graphite if its state of charge is higher than 50%, i.e., only if all lithium is contained in the LiC_6 and the LiC_{12} phases. In addition, it needs to be taken into account that the graphite electrode is typically capacitively oversized [47]. Clearly defined LiC_6 and LiC_{12} diffractions without visible diffractions from lower lithiated phases and graphite in the discharged state can only be observed for the stored/cycled MCMB cells. In this case, the sum of the LiC_6 and LiC_{12} molar fractions equals the total amount of graphite active material, so that the active lithium inventory denoted as $L_{\text{LiC}_6/\text{LiC}_{12}}$ and can be calculated by

$$L_{\text{LiC}_6/\text{LiC}_{12}} = [y(\text{LiC}_6)/2 + 50\%]*B \quad (2)$$

where $y(\text{LiC}_6)$ is the molar fraction of LiC_6 in % (ranging from 12% to 23%, as shown in Table 4) and B is the anode/cathode balancing factor, which is 1.25 for the cells investigated in this study. Due to the capacitively larger graphite anode (i.e., the balancing factor of >1), a LiC_6 phase fraction of 100% cannot be obtained even if 100%

of the electrochemically active lithium were still present (based on Eq. (2), the maximum molar fraction of LiC_6 for $B = 1.25$ is 60%). Accordingly, a $\text{LiC}_6/\text{LiC}_{12}$ ratio of 12/88 as determined for the cycled MCMB cell in its charged state corresponds to $y(\text{LiC}_6) = 12\%$, which based on Eq. (2) equates to an active lithium inventory of $L_{\text{LiC}_6/\text{LiC}_{12}} = 70\%$. The active lithium inventory values determined by neutron diffraction analysis either from the LFP/FP ratio measured in discharged cells ($L_{\text{LFP/FP}}$; using Eq. (1)) or from the $\text{LiC}_6/\text{LiC}_{12}$ ratio measured in charged cells ($L_{\text{LiC}_6/\text{LiC}_{12}}$; using Eq. (2)) are summarized in the second and third column of Table 5.

The fourth and fifth column in Table 5 shows the electrochemically determined remaining discharge capacities (RDC) of the different cells, expressed as percentage of the initial theoretical capacity (1.678 Ah; see Fig. 1). The values in the fourth column (RDC_{1C}) were measured with the same discharge procedure which was used for the long term cycling by the battery producer (also shown in the third column of Table 1). The values in the fifth column (RDC_{CCCV}) were measured with the same discharge procedure which was used to prepare the cells for neutron diffraction experiments in the discharged state (same charging procedure, but followed by a C/5 discharge to 2.0 V with a CV hold until C/20), so that they can be directly compared to the $L_{\text{LFP/FP}}$ values. In summary, the RDC_{CCCV} values can be used for comparison with the active lithium inventory determined by the LFP/FP ratio and the $\text{LiC}_6/\text{LiC}_{12}$ ratio. On the other hand, the RDC_{1C} values can be used to compare the capacity of the stored and cycled cells to that of the preformed cells (for which no RDC_{CCCV} data is available). Note, that the discharge capacities measured with the two different protocols (i.e., RDC_{1C} and RDC_{CCCV}) are very similar, thus confirming that impedance build-up effects (i.e. increased impedance over time, which would result in a so-called capacity roll-over) [36] do not contribute significantly to the capacity fading, as was already discussed in the previous section.

4. Discussion

In the following sections the different mechanisms contributing to capacity fading will be discussed for i) the preformed cells which only show formation loss, ii) the stored cells which show a sum of formation loss and calendar aging, and, iii) the cycled cells which show a sum of the formation loss and cyclic aging. For the preformed cells it is only possible to compare their discharge capacity to the theoretical LFP capacity in the pristine cells, as no neutron diffraction experiments were carried out in between formation and storage/long term cycling (see Fig. 1). In contrast, for the stored and

cycled cells it is possible to compare neutron diffractograms and the corresponding LFP/FP and $\text{LiC}_6/\text{LiC}_{12}$ fractions to their electrochemically determined capacities.

4.1. Formation loss

After formation, the remaining discharge capacities RDC_{1C} are 73.3% for the MCMB cells and 68.5% for the needle coke cells (Table 5). Accordingly, the irreversible capacity loss during the formation process amounts to 26.7% for the MCMB cells and 31.5% for the needle coke cells. The irreversible capacity loss in the first cycles is generally exclusively caused by the consumption of active lithium for the solid electrolyte interphase (SEI) formation on the graphite electrode. A capacity loss during formation on the order of 30% is surprisingly high, as typical graphite anode materials usually show a significantly lower first-cycle irreversible capacity loss of about 10% [49,50]. Considering the oversized anode (balancing factor of 1.25), one would expect an irreversible capacity of about 12.5% of the theoretical cell capacity. The reason for the much higher capacity loss during formation is unclear, but must be related to the specific formation procedure applied to these commercial cells, which consumes more active lithium and thus forms a thicker SEI, presumably in order to reduce subsequent capacity losses during cell cycling. In this way, one obtains a cell with a lower initial capacity, but lower capacity fading during storage/cycling, as exemplified by the very low relative capacity loss of only 8% for the MCMB cell during the subsequent 4750 cycles (Fig. 4a). The relatively high formation loss in these commercial cells is an interesting finding as this information is usually not readily available for commercial cells, for which only a nominal capacity in units of Ah is stated, without revealing what fraction of the active cathode material is actually used (i.e., in terms of $\text{mAh g}^{-1}_{\text{LFP}}$). This “shifting” of capacity loss into the formation process also has to be taken into account when comparing the cycling performance of commercial cells with lab-built Swagelok or coin cells. In academic studies, a typical formation procedure consists of a few slow cycles (e.g. C/10 or C/20) at room temperature, during which the irreversible capacity loss would range from 10 to 15%. Further capacity losses due to continuing growth of the anode SEI would then take place during cell cycling and would therefore lead to a higher apparent capacity fading in comparison to commercial cells with identical cell chemistry.

Unfortunately, the formation procedures for commercial cells are essentially always proprietary, and the question remains, whether the formation related capacity losses of 26.7% and 31.5% observed for the graphite/LFP cells investigated in the present study are representative of commercial cells or whether they are unusually high. While this information is not made public by battery producers, some answers can be found in two other neutron diffraction studies, which report the LFP/FP ratios for “fresh” (meaning “preformed” in our nomenclature) commercially produced graphite/LFP cells. Rodriguez et al. found a LFP/FP ratio of 75/25 for a 2.6 Ah 18650-type cell and Bobrikov et al. found a value of 57/43 (with a significant uncertainty) for a 2.0 Ah prismatic cell [28,30]. The corresponding formation related capacity losses of 25% and $43 \pm 10\%$, respectively, indicate that the formation losses of the cells investigated in our study seem to be within the range observed for other commercial graphite/LFP cells.

4.2. Calendar aging

Upon two years of storage (at 20% SOC, 23 °C), the remaining discharge capacity RDC_{1C} of the MCMB cell increases from 73.3% to 74.4% (Table 5), which means that there is no calendar aging for this cell. The reason for the slight capacity increase upon storage is

Table 5

Active lithium inventory derived from the molar LFP/FP ratio in the discharged cells ($L_{\text{LFP/FP}}$) and the $\text{LiC}_6/\text{LiC}_{12}$ ratio in the charged cells ($L_{\text{LiC}_6/\text{LiC}_{12}}$), both determined from the neutron diffraction data. The remaining capacities after storage/cycling are the electrochemically determined discharge capacities normalized by the theoretical capacity of the pristine cells (1.678 Ah) and obtained from two different cycling procedures: i) RDC_{1C} is the discharge capacity obtained when cycling the cells at the same procedure as used in the long term cycling test (Fig. 4: CC charge at 1C with a CV hold at 3.6 V until a C/20 cut-off and 1C discharge to 2.0 V at 23 °C); ii) RDC_{CCCV} is the discharge capacity obtained with the same charging procedure, but followed by a C/5 discharge to 2.0 V with a CV hold until C/20.

State of cells	Lithium inventory		Remaining capacity	
	$L_{\text{LFP/FP}}$	$L_{\text{LiC}_6/\text{LiC}_{12}}$	RDC_{1C}	RDC_{CCCV}
Preformed MCMB	—	—	73.3%	—
Stored MCMB	75%	76%	74.4%	75.2%
Cycled MCMB	67%	70%	67.3%	67.0%
Preformed needle coke	—	—	68.5%	—
Stored needle coke	58%	n.a.	61.1%	61.8%
Cycled needle coke	55%	n.a.	52.8%	53.0%

consistent with data recently published by Kassem et al. and Li et al., who also found a slight capacity increase in commercially produced cylindrical graphite/LFP cells after one year of storage at different SOCs [51–53]. For the stored MCMB cell, the remaining discharge capacity of $RDC_{CCCV} = 75.2\%$ is in excellent agreement with the active lithium inventory determined by neutron diffraction from the LFP/LP ratio of $Li_{LFP/FP} = 75\%$ and from the LiC_6/LiC_{12} ratio of $Li_{LiC_6/LiC_{12}} = 76\%$ (Table 5), meaning that active lithium loss accounts for the entire capacity loss of the stored MCMB cell.

In contrast, the needle coke cell shows a significant calendar aging, with the remaining discharge capacity decreasing from $RDC_{1C} = 68.5\%$ after formation to 61.1% after storage (Table 5). The active lithium inventory determined by the LFP/FP ratio of $Li_{LFP/FP} = 58\%$ slightly overestimates the capacity loss in comparison to the electrochemically observed remaining capacity of $RDC_{CCCV} = 61.8\%$. There is no indication for the contribution of particle deactivation by electronic/ionic insulation to capacity fading, as no $LiFePO_4$ is observed in the charged cell and no LiC_6/LiC_{12} (or other lithiated phases) are observed in the discharged cell. One can conclude that active lithium loss is most likely also the sole contributor to capacity fading in the stored needle coke cell, which is again consistent with results published by Kassem et al. [52,53]. The difference between the lithium inventory $Li_{LFP/FP}$ and the remaining discharge capacity is probably due to the fitting error of the neutron diffraction data, which is estimated to be about 3% from the fitting software for each of the fitted phases (LFP and FP in this case).

At the current stage, the reason for the different calendar aging behavior of the stored MCMB and the stored needle coke cells is not clear. Interestingly, the stored MCMB cell shows both a higher polarization (Fig. 4b) and a higher charge transfer resistance (Fig. 4c) than the stored needle coke cell ($25.7\text{ m}\Omega$ vs. $14.0\text{ m}\Omega$, respectively). This might be an indication for the formation of a more passivating SEI layer on the MCMB in comparison to the needle coke, which on the one hand increases the charge transfer resistance, but on the other hand more effectively suppresses further electrolyte reduction, thereby lowering the corresponding capacity loss. Or, in other words, the higher charge transfer resistance and lower calendar aging of the MCMB cell might be two sides of the same coin. Furthermore, the different calendar aging might also be influenced by the nature of the exposed graphite planes which strongly depend on the local arrangement of crystallite grains [49]. In normal flake-like graphite as needle coke, the majority (>90%) of the exposed graphite layers are basal planes [54] while MCMB shows a higher fraction of exposed edge planes [49]. It is known that the SEI on edge and basal planes differs both in chemical composition and especially thickness [55–57]. Based on x-ray photoelectron spectroscopy (XPS) Peled et al. reported a thickness of 2 nm for basal and 30 nm for edge plane SEI [56]. The thicker SEI on the edge plane is probably a consequence of either solvent co-intercalation during charge, which is not possible on basal planes [58,59], and/or the constant expansion and contraction of graphite perpendicular to the edge planes during cycling. Newman and co-workers showed that there is also a difference in the passivation behavior of the edge and basal plane SEI on highly oriented pyrolytic graphite (HOPG) and they concluded that the SEI on basal planes might be thin enough to permit limited electron tunneling [60]. Accordingly, the higher fraction of basal planes might contribute to the significant calendar aging of the stored needle coke cell while the stored MCMB cell does not show any calendar aging. We are currently carrying out further experiments to thoroughly investigate which chemical, physicochemical, and/or structural/mechanical properties are responsible for the different passivation and calendar aging behavior of the MCMB and needle coke graphite.

4.3. Cyclic aging

Upon cycling for 4750 cycles, the remaining discharge capacity RDC_{1C} decreases from 73.3% to 67.3% for the MCMB cell (Table 5), corresponding to a capacity loss of 6% if referenced to the theoretical capacity or of 8.2% if referenced to the capacity of the preformed cell (Table 1). The essentially perfect correspondence of the active lithium inventory deduced from the LFP/LP ratio ($Li_{LFP/FP} = 67\%$ with the remaining discharge capacity $RDC_{CCCV} = 67.0\%$ clearly indicates that the capacity fading during cycling of the MCMB cell can be accounted quantitatively by active lithium loss, excluding effects caused by particle isolation/degradation and impedance growth effects.

For the cycled needle coke cell, the remaining discharge capacity RDC_{1C} decreases from 68.5% to 52.8%, corresponding to a capacity loss of 15.7% if referenced to the theoretical capacity or of 23.1% if referenced to the preformed cell. In principle, these capacity losses contain contributions from calendar aging and cyclic aging, but a clear deconvolution is not possible on the basis of our experiments. The comparison of the active lithium inventory deduced from the LFP/LP ratio of $Li_{LFP/FP} = 55\%$ with the remaining discharge capacity $RDC_{CCCV} = 53.0\%$ shows that, within the error of the neutron diffraction analysis, the entire capacity fading can be accounted for by active lithium loss. And again, there is no indication for the occurrence of other aging mechanisms, as no new phases in the diffraction patterns emerge, the lattice parameters of all active materials stay constant and no lithium containing inactive particles are observed.

The reason for the faster loss of active lithium upon cycling in the needle coke cell in comparison to the MCMB cell is currently being investigated in our labs. In this respect, it is very important to understand which processes contribute to the loss of active lithium in each cell. The linear decrease of the cell capacity with cycling number as observed for the MCMB cell (Fig. 4a) is typical for active lithium loss due to the constant repair of a small fraction of the anode SEI caused by the slight expansion and contraction of the graphite particles upon lithium intercalation and deintercalation [61]. In contrast, the higher initial rate of capacity fading upon cycling observed for the needle coke cell (Fig. 4a) might be an indication for the presence of a second process contributing to the loss of active lithium during the initial 1000 cycles, for example partial lithium plating during charge.

4.4. Active lithium loss analysis via the LFP/FP ratio versus the LiC_6/LiC_{12} ratio

For the graphite/LFP cells investigated in this study, the lithium inventory can, in general, be determined by neutron diffraction based on the molar ratio of LFP/FP (measured in the discharged state) or through the LiC_6/LiC_{12} ratio (measured in the charged state). Theoretically, the values of $Li_{LFP/FP}$ and $Li_{LiC_6/LiC_{12}}$ should give identical results, as they both determine the same parameter, namely the amount of active lithium. Indeed, for the MCMB cells, the $Li_{LFP/FP}$ and $Li_{LiC_6/LiC_{12}}$ values agree within 1% for the stored cell and within 3% for the cycled cell (Table 5). Note, that one would only expect identical results for the $Li_{LFP/FP}$ and $Li_{LiC_6/LiC_{12}}$ values for cells in which active lithium loss is the only mechanism contributing to capacity fading, as is the here. While LFP/FP and LiC_6/LiC_{12} ratios should ideally give identical results, there are some considerations which might render one of them advantageous for LFP/FP based cells.

As already discussed, the lithiation/delithiation process of graphite is only a two phase mechanism for higher lithiation degrees ($x > 0.5$ in Li_xC_6) [47,48]. Accordingly, the lithium inventory can only be determined through the LiC_6/LiC_{12} ratio as long as the

cell capacity is higher than $0.5 \cdot Q_{\text{theo}} \cdot B$, where Q_{theo} is the theoretical capacity of the pristine cell and B is the cell balancing factor. This limitation is the reason why the $\text{LiC}_6/\text{LiC}_{12}$ ratio cannot be determined for the needle coke cells in the present study. In contrast, the lithiation/delithiation of LFP is a two phase mechanism of triphylite (LiFePO_4) and the heterosite (FePO_4) over the entire capacity range; therefore, the triphylite/heterosite phase ratio can be used for the determination of the $\text{Li}_{\text{LFP}}/\text{FP}$ independent of the remaining capacity. Another advantage of the analysis via the LFP/FP ratio over that of the $\text{LiC}_6/\text{LiC}_{12}$ ratio is that the former can also be used to determine the lithium inventory and the active lithium loss, if the anode/cathode balancing factor is unknown, which is usually the case for commercial cells (compare equations (1) and (2)).

5. Conclusion and outlook

In this study, the capacity fading processes in four commercially produced 18650-type graphite/LFP cells, which differed either in the kind of graphite active material or the applied type of aging, were investigated *in situ* with neutron diffraction. All four cells showed a rather high formation loss in the order of 30% (27% for an MCMB based anode and 31% for a needle coke based anode) and excellent cycling stability thereafter, with relative capacity losses (referring to the capacity after formation) of only $\approx 8\%$ for the MCMB cell and $\approx 23\%$ for the needle coke cell during 4750 cycles. Upon two years of storage, the MCMB cell showed no measurable capacity loss, while the needle coke cell lost $\approx 11\%$ of its relative capacity.

The comparison of neutron diffraction experiments in the charged and discharged state with electrochemical characterization reveals that the entire capacity loss upon formation, cycling, and storage is solely due to active lithium loss. Based on the neutron diffractograms, the contribution of other aging mechanisms like deactivation and active material isolation/destruction can be excluded. The slower calendar aging of the MCMB cell in comparison to the needle coke cell is probably due to the formation of an SEI layer which provides better passivation, reflected by the higher cell impedance of the MCMB cells. The slower cyclic aging of the MCMB cell in comparison to the needle coke cell is probably caused by different mechanisms of active lithium loss: The decrease of discharge capacity with cycle number indicates that in the MCMB cell the entire active lithium loss is caused by ongoing SEI repair, while in the needle coke cell a second mechanism might contribute to active lithium loss in the first 1000 cycles, the origin of which is currently under investigation.

Acknowledgements

This work was financially supported by the Bavarian Ministry of Economic Affairs and Media, Energy and Technology under the auspices of the EEBatt project. The authors thank the Heinz Maier-Leibnitz Zentrum (MLZ) for granting beam time at FRM II.

Appendix A. Supplementary data

Supplementary data related to this article can be found at <http://dx.doi.org/10.1016/j.jpowsour.2017.01.134>.

References

- [1] B. Nykvist, M. Nilsson, *Nat. Clim. Chang.* 5 (2015) 329–332.
- [2] J.-M. Tarascon, *Philos. Trans. A. Math. Phys. Eng. Sci.* 368 (2010) 3227–3241.
- [3] F.T. Wagner, B. Lakshmanan, M.F. Mathias, *J. Phys. Chem. Lett.* 1 (2010) 2204–2219.
- [4] D. Andre, S.-J. Kim, P. Lamp, S.F. Lux, F. Maglia, O. Paschos, B. Stiaszny, *J. Mater.*

- Chem. A* 3 (2015) 6709–6732.
- [5] S.J. Harris, P. Lu, *J. Phys. Chem. C* 117 (2013) 6481–6492.
- [6] USABC, USABC Goals for Advanced Batteries for EVs - CY2020 Commercialization, can be found under, 2015. http://www.energy.gov/sites/prod/files/2014/05/f15/APR13_Energy_Storage_d_III_Adv_Battery_Dev_0.pdf.
- [7] U.S. Department of Energy, Grid Energy Storage, can be found under http://energy.gov/sites/prod/files/2014/09/f18/Grid_Energy_Storage_December_2013.pdf, accessed September 2016.
- [8] P.P.R.M.L. Harks, F.M. Mulder, P.H.L. Notten, *J. Power Sources* 288 (2015) 92–105.
- [9] J. Wandt, P. Jakes, J. Granwehr, H.A. Gasteiger, R.-A. Eichel, *Angew. Chem. Int. Ed.* 55 (2016) 6892–6895.
- [10] X.-L. Wang, K. An, L. Cai, Z. Feng, S.E. Nagler, C. Daniel, K.J. Rhodes, A.D. Stoica, H.D. Skorpenske, C. Liang, et al., *Sci. Rep.* 2 (2012) 1–7.
- [11] J. Wandt, A. Freiberg, R. Thomas, Y. Gorlin, A. Siebel, R. Jung, H.A. Gasteiger, M. Tromp, *J. Mater. Chem. A* 4 (2016) 18300–18305.
- [12] Y. Gorlin, A. Siebel, M. Piana, T. Huthwelker, H. Jha, G. Monsch, F. Kraus, H.A. Gasteiger, M. Tromp, *J. Electrochem. Soc.* 162 (2015) A1146–A1155.
- [13] J. Wandt, C. Marino, P. Jakes, R. Eichel, H.A. Gasteiger, J. Granwehr, *Energy Environ. Sci.* 8 (2015) 1358–1367.
- [14] F. Poli, J.S. Kshetrimayum, L. Monconduit, M. Letellier, *Electrochem. Commun.* 13 (2011) 1293–1295.
- [15] N. Tsiouvaras, S. Meini, I. Buchberger, H.A. Gasteiger, *J. Electrochem. Soc.* 160 (2013) A471–A477.
- [16] A. Senyshyn, M.J. Mühlbauer, O. Dolotko, M. Hofmann, H. Ehrenberg, *Sci. Rep.* (2015) 1–9.
- [17] R.S. Rubino, H. Gan, E.S. Takeuchi, *J. Electrochem. Soc.* 148 (2001) A1029–A1033.
- [18] T. Waldmann, S. Gorse, T. Samtleben, G. Schneider, V. Knoblauch, M. Wohlfahrt-Mehrens, *J. Electrochem. Soc.* 161 (2014) A1742–A1747.
- [19] M. Fleckenstein, O. Böhlen, M.A. Roscher, B. Baker, *J. Power Sources* 196 (2011) 4769–4778.
- [20] M.A. Rodriguez, D. Ingersoll, D.H. Doughty, *JCPDS Adv. X-ray Anal.* 45 (2002) 182–187.
- [21] M.A. Rodriguez, D. Ingersoll, S.C. Vogel, D.J. Williams, *Electrochem. Solid-State Lett.* 7 (2004) A8.
- [22] N. Sharma, V.K. Peterson, M.M. Elcombe, M. Avdeev, A.J. Studer, N. Blagojevic, R. Yusoff, N. Kamarulzaman, *J. Power Sources* 195 (2010) 8258–8266.
- [23] O. Dolotko, A. Senyshyn, M.J. Mühlbauer, K. Nikolowski, F. Scheiba, H. Ehrenberg, *J. Electrochem. Soc.* 159 (2012) A2082–A2088.
- [24] A. Senyshyn, M.J. Mühlbauer, K. Nikolowski, T. Pirling, H. Ehrenberg, *J. Power Sources* 203 (2012) 126–129.
- [25] L. Cai, K. An, Z. Feng, C. Liang, S.J. Harris, *J. Power Sources* 236 (2013) 163–168.
- [26] O. Dolotko, A. Senyshyn, M.J. Mühlbauer, K. Nikolowski, H. Ehrenberg, *J. Power Sources* 255 (2014) 197–203.
- [27] V. Zinth, C. von Lüders, M. Hofmann, J. Hattendorff, I. Buchberger, S. Erhard, J. Rebelo-Kormmeier, A. Jossen, R. Gilles, *J. Power Sources* 271 (2014) 152–159.
- [28] M.A. Rodriguez, M.H. Van Benthem, D. Ingersoll, S.C. Vogel, H.M. Reiche, *Powder Diffr.* 25 (2010) 143–148.
- [29] C.W. Hu, N. Sharma, C.-Y. Chiang, H.-C. Su, V.K. Peterson, H.W. Hsieh, Y.F. Lin, W.C. Chou, B.Y. Shew, C.H. Lee, *J. Power Sources* 244 (2013) 158–163.
- [30] I.A. Bobrikov, A.M. Balagurov, C.W. Hu, C.H. Lee, T.Y. Chen, S. Deleg, D.A. Balagurov, *J. Power Sources* 258 (2014) 356–364.
- [31] A. Senyshyn, M.J. Mühlbauer, O. Dolotko, M. Hofmann, T. Pirling, H. Ehrenberg, *J. Power Sources* 245 (2014) 678–683.
- [32] A.J. Smith, J.C. Burns, X. Zhao, D. Xiong, J.R. Dahn, *J. Electrochem. Soc.* 158 (2011) A447–A452.
- [33] J.C. Burns, D.A. Stevens, J.R. Dahn, *J. Electrochem. Soc.* 162 (2015) A959–A964.
- [34] R. Bernhard, S. Meini, H.A. Gasteiger, *J. Electrochem. Soc.* 161 (2014) A497–A505.
- [35] R.P. Day, J. Xia, R. Petibon, J. Rucsa, H. Wang, A.T.B. Wright, J.R. Dahn, *J. Electrochem. Soc.* 162 (2015) A2577–A2581.
- [36] J.C. Burns, A. Kassam, N.N. Sinha, L.E. Downie, L. Solnickova, B.M. Way, J.R. Dahn, *J. Electrochem. Soc.* 160 (2013) A1451–A1456.
- [37] K. Ishidzu, Y. Oka, T. Nakamura, *Solid State Ionics* 288 (2016) 176–179.
- [38] M. Koltypin, D. Aurbach, L. Nazar, B. Ellis, *Electrochem. Solid-State Lett.* 10 (2007) A40.
- [39] H. Zheng, Q. Sun, G. Liu, X. Song, V.S. Battaglia, *J. Power Sources* 207 (2012) 134–140.
- [40] C. Delacourt, A. Kwong, X. Liu, R. Qiao, W.L. Yang, P. Lu, S.J. Harris, V. Srinivasan, *J. Electrochem. Soc.* 160 (2013) A1099–A1107.
- [41] M. Hoelzel, A. Senyshyn, N. Juenke, H. Boysen, W. Schmahl, H. Fuess, *Nucl. Instrum. Methods Phys. Res. Sect. A Accel. Spectrom. Detect. Assoc. Equip.* 667 (2012) 32–37.
- [42] R. Gilles, B. Krimmer, H. Boysen, H. Fuess, *Appl. Phys. A* 74 (2002) S148–S150.
- [43] T. Roisnel, J. Rodríguez-Carvajal, *Mater. Sci. Forum* 378–381 (2001) 118–123.
- [44] S. Solchenbach, D. Pritzl, E.J.Y. Kong, J. Landesfeind, H.A. Gasteiger, *J. Electrochem. Soc.* 163 (2016) A2265–A2272.
- [45] M. Gaberscek, J. Moskon, B. Erjavec, R. Dominko, J. Jamnik, *Electrochem. Solid-State Lett.* 11 (2008) A170–A174.
- [46] J. Landesfeind, J. Hattendorff, A. Ehl, W.A. Wall, H.A. Gasteiger, *J. Electrochem. Soc.* 163 (2016) A1373–A1387.
- [47] J.R. Dahn, *Phys. Rev. B* 44 (1991) 9170–9177.
- [48] A. Senyshyn, O. Dolotko, M.J. Mühlbauer, K. Nikolowski, H. Fuess, H. Ehrenberg, *J. Electrochem. Soc.* 160 (2013) A3198–A3205.

- [49] G. Chung, S. Jun, K. Lee, M. Kim, J. Electrochem. Soc. 146 (1999) 1664–1671.
- [50] S. Hossain, Y.K. Kim, Y. Saleh, R. Loutfy, J. Power Sources 114 (2003) 264–276.
- [51] D. Li, D.L. Danilov, J. Xie, L. Raijmakers, L. Gao, Y. Yang, P.H.L. Notten, Electrochim. Acta 190 (2016) 1124–1133.
- [52] M. Kassem, J. Bernard, R. Revel, S. Pélissier, F. Duclaud, C. Delacourt, J. Power Sources 217 (2012) 574.
- [53] M. Kassem, C. Delacourt, J. Power Sources 235 (2013) 159–171.
- [54] K. Zaghib, G. Nadeau, K. Kinoshita, J. Electrochem. Soc. 147 (2000) 2110.
- [55] D. Bar-Tow, E. Peled, L. Burstein, J. Electrochem. Soc. 146 (1999) 824.
- [56] E. Peled, D. Bar Tow, A. Merson, A. Gladkich, L. Burstein, D. Golodnitsky, J. Power Sources 97–98 (2001) 52–57.
- [57] E. Peled, D. Golodnitsky, A. Ulus, V. Yufit, Electrochim. Acta 50 (2004) 391–395.
- [58] J.O. Besenhard, M. Winter, J. Yang, W. Biberacher, J. Power Sources 54 (1995) 228–231.
- [59] M. Inaba, Z. Siroma, A. Funabiki, Z. Ogumi, T. Abe, Y. Mizutani, M. Asano, Langmuir 12 (1996) 1535–1540.
- [60] M. Tang, J. Newman, J. Electrochem. Soc. 159 (2012) A1922–A1927.
- [61] D. Li, D.L. Danilov, L. Gao, Y. Yang, P.H.L. Notten, Electrochim. Acta 190 (2016) 445–455.